ACS Catalysis

pubs.acs.org/acscatalysis
Research Article

A Supportive Support: The Important Role of Porous Supports in Plasma-Catalytic Ammonia Synthesis

Katja Vodlan, Weitao Wang, Michal Mazur, Daria Sudakova, Jens-Peter Baernholdt Haraldsted, Anej Blažič, Janvit Teržan, Xin Tu,* Blaž Likozar,* and Matej Huš*

Cite This: *ACS Catal.* 2026, 16, 9887−9901
Read Online

ABSTRACT: Plasma catalysis is a promising method for synthesizing ammonia, utilizing dielectric barrier discharge (DBD) to supply the energy required for N≡N bond cleavage. Although efficient, the process is hindered by ammonia dissociation in the plasma zone, which must be prevented. Micro- and mesoporous frameworks can mitigate this issue by protecting the formed ammonia from immediate decomposition. However, their effects extend beyond porosity, as the presence of acidic sites significantly improves ammonia yields, refuting the idea of a simple spectator or inert support. Here, we systematically evaluate five different MCM materials—MWW zeolites MCM-22, MCM-36, and MCM-56, as well as mesoporous silicas MCM-41 and MCM-48—both as pristine materials and as supported NiO catalysts for plasma-catalytic ammonia synthesis. To quantify the importance of the acidic properties of the catalyst, experiments were conducted at constant discharge power and under a power-swing regime. In power-swing experiments, NiO/MCM-56, which has the highest amount of moderate acidic sites, achieved 1.5 times higher ammonia concentration than the best-performing catalysts at constant discharge power. We show that tailored acidic properties of the support further enhance the shielding effect, enabling efficient sorption-enhanced plasma-catalytic ammonia synthesis by using plasma power modulation rather than external heating for ammonia desorption. Three distinct properties required of a "good catalyst" are identified: porous structure, active phase location and, most importantly, surface acidity.

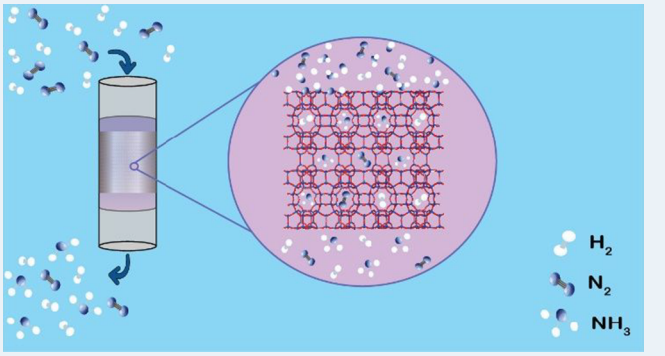

KEYWORDS: *ammonia, plasma catalysis, sorption, supported catalyst, power-swing*

1. INTRODUCTION

Ammonia is one of the most widely produced chemicals,[1−3] primarily through the conventional Haber–Bosch process.[4,5] To meet its high energy demands, this process relies heavily on fossil fuels, resulting in significant CO_2 emissions.[6] Additionally, ammonia production is highly centralized, as conventional production is only profitable at a large scale, leading to additional cost and CO_2 emissions due to transport.[7,8] While demand from existing sectors is increasing, ammonia is also making inroads into the energy sector as a hydrogen carrier,[9−11] marine fuel,[12] and energy storage medium.[13] Since the Haber–Bosch process is already one of the largest sources of greenhouse gas emissions and global energy consumption, it is of great importance to develop alternative methods for small-scale ammonia production under milder conditions.[14] Reaction systems using non-thermal plasma have been widely researched for this purpose.[15−17] Plasma generates highly reactive species, such as high-energy electrons, vibrationally and electronically excited molecules, ions, and radicals, allowing efficient ammonia generation even at ambient conditions.[18] Plasma systems have short response times and can therefore operate on intermittent renewable energy sources. Combined with water electrolysis, atmospheric pressure plasma systems could enable clean, carbon-free ammonia generation on a small scale.[14,15,19]

Despite this potential, plasma-catalytic systems are limited by low energy efficiencies, mainly due to dissociation of produced ammonia in the plasma region.[15,20] In order to overcome this limitation, microporous materials such as zeolites[21−23] and metal–organic frameworks,[24] as well as mesoporous silicas,[20,25−27] have been tested. Research on the activity of porous materials for DBD plasma-catalytic ammonia formation has mostly focused on the textural properties of the materials. Gorky et al.[23] studied SAPO catalysts with different pore sizes and observed an enhanced activity for SAPO-11(3.9 Å) and SAPO-34 (3.8 Å),

Received: January 6, 2026
Revised: April 29, 2026
Accepted: May 1, 2026
Published: May 18, 2026

https://doi.org/10.1021/acscatal.6c00096
ACS Catal. 2026, 16, 9887−9901

but not for SAPO-56 (3.6 Å), as its pore size is smaller than the kinetic radius of nitrogen. This finding demonstrated the importance of diffusion of active species into the pores of the material. Similarly, Gorky[28] compared the activities of zeolite 4A, zeolite 5A, and zeolite beta with respect to pore size.

The ability to form plasma is limited to the pores with diameter greater than or equal to the Debye length.[26] For atmospheric dielectric barrier discharge (DBD) plasmas, the threshold diameter is usually larger than the pore size of micro- and mesoporous materials.[29] Therefore, these materials can shield the ammonia produced inside the pores from dissociation in plasma,[20,26,27] while still promoting diffusion of plasma-activated species to the active sites.[21,25,30,31] Wang et al.[20] studied the shielding effect of MCM(Mobil Composition of Matter)–41 support in a water-cooled DBD plasma reactor system, which maintained the temperature at approximately 35 °C, demonstrating improved ammonia yield due to the diffusion of ammonia into the mesopores of the catalyst. However, this effect may not be as pronounced in a typical DBD reactor system, where, depending on the discharge power and the packing material, the temperature in the discharge region can exceed 100 °C.[32−38] To promote the shielding properties of the porous support in such reactor systems, moderate acidic sites of zeolites could be beneficial. Rouwenhorst et al.[22] demonstrated sorption-enhanced plasma-catalytic ammonia synthesis using zeolite 4A. The adsorbed ammonia was recovered in situ using temperature-swing, which doubled the energy yield. Similarly, Arumuganainar et al.[26] introduced acidic sites into pure mesoporous silica SBA-15 by coating it with alumina using wetness impregnation and recovered ammonia by temperature-programmed desorption.

However, apart from those studies, research on the utilization of acidic properties for plasma-catalytic ammonia production remains scarce despite its potential. In addition to their high surface accessibility, MWW zeolites are well suited for evaluating the influence of textural and acidic properties because of their unique hierarchical structures.[39] These zeolites consist of MWW layers containing 10-ring medium pore size sinusoidal channels and 12-ring cavities on the surface.[40] The combination of the channel system and multiple interlayer condensation degrees results in a diverse MWW family of zeolites with different levels of structural order and interlayer spacing.[41,42] MWW zeolites are synthesized from MCM-22(P), a layered precursor that consists of stacked but not fully covalent 2.5 nm thick crystalline layers.[43] These layers are held together by hydrogen bonding and an organic pore-directing agent between them.[44] MCM-22(P) can be further transformed into 3D zeolite MCM-22 via calcination, as the organic pore-directing agent is removed and the silanol groups between the layers are fully condensed.[45] Furthermore, MCM-22(P) can be transformed via swelling with surfactant followed by pillaring into MCM-36[46] or via mild acid treatment into MCM-56. MCM-36 consists of microporous layers with amorphous silica pillars that create mesopores between the layers, and can be tuned by the surfactant size, used for swelling. On the other hand, MCM-56 consists of randomly stacked MWW layers with limited interlayer connectivity.[46]

To better understand the influence of the porous support on DBD plasma-catalytic ammonia production, we studied the activity of layered zeolites MCM-22, MCM-36, and MCM-56 and compared them with MCM-41. Additionally, mesoporous silica MCM-48, which has distinct textural properties from MCM-41, was also tested. The porous supports were also used to synthesize supported NiO variants of the catalysts. The trends in catalytic performances of the tested materials were explained using ammonia temperature-programmed desorption and hydrogen temperature-programmed reduction. Three catalysts with different acidic properties were then tested in the power-swing experiments to demonstrate the effects of sorption-enhanced plasma-catalytic synthesis of ammonia and decouple the physical shielding from the sorption-enhanced mechanism.

2. EXPERIMENTAL SECTION

2.1. Materials

Sodium hydroxide (NaOH, 50% solution in water) was purchased from Acros Organics. Tetraethyl orthosilicate-TEOS ($Si(OC_2H_5)_4$, 99.9%) was purchased from Thermo Scientific Chemicals. Cetyltrimethylammonium chloride, CTAC ($CH_3(CH_2)_{15}N(Cl)(CH_3)_3$, 25 wt % in water), hexadecyltrimethylammonium bromide, CTAB($CH_3(CH_2)_{15}N(Br)(CH_3)_3$), sodium aluminate ($NaAlO_2$:50–56% Al_2O_3, 40–45% Na_2O), ULTRASIL VN 3 (SiO_2), LUDOX AS-30 (colloidal silica, SiO_2), hexamethyleneimine, HMI ($C_6H_{13}N$), Ambersep 900 Ion Exchange Resin, and MCM-48 were purchased from Sigma Aldrich. Ammonium hydroxide (NH_4OH, 30–33%) was purchased from Carl Roth, and nickel(II) chloride hexahydrate ($NiCl_2{\cdot}6H_2O$, 98%) was purchased from KEMIKA.

2.2. Porous Support Synthesis

MCM-22(P) was synthesized via the hydrothermal method. Deionized water, 50% NaOH solution, and $NaAlO_2$ were combined in a beaker and mixed thoroughly. LUDOXAS-30 colloidal silica was then added, and the mixture was stirred until a homogeneous gel was formed. HMI was subsequently introduced to the gel. After 10 min of stirring, the resulting mixture was transferred to a Parr autoclave and heated at 143 °C under stirring at 400 rpm for 5 days. The solid product was recovered by filtration, washed with deionized water, and dried overnight at 60 °C.

MCM-22 was obtained by a two-step calcination of MCM-22(P). The sample was first calcined under a nitrogen atmosphere at 480 °C for 3 h with a heating rate of 1 °C /min, followed by calcination in air at 540 °C for 8 h at the same rate.

MCM-36 was synthesized from the precursor MCM-22(P). In the first step, CTAB was converted to its hydroxide form (CTAOH, $CH_3(CH_2)_{15}N(OH)(CH_3)_3$) by ion exchange using Ambersep 900 Ion Exchange Resin. A 100 mL aliquot of 25 wt % CTAB solution was mixed with 70 g of ion exchange resin and stirred for 4 h. The mixture was then filtered to obtain the CTAOH solution. For the swelling step, 1 g of MCM-22(P) was added to 4 g of deionized water, followed by 20 g of the prepared CTAOH solution. The suspension was stirred overnight at room temperature. The resulting mixture was decanted, washed three times with deionized water, and dried. In the pillaring step, the swollen material was mixed with 30 g of TEOS and heated under reflux at 90 °C overnight. The mixture was separated by centrifugation, and the supernatant was decanted. The solid was left in an inverted tube to evaporate any residual TEOS, then dispersed in 20 mL of deionized water, and stirred overnight. The product was again separated by centrifugation, dried at 60 °C, and finally calcined in air at 540 °C for 5 h with a heating rate of 1 °C/min.

MCM-41 was synthesized using a method described elsewhere.[20] Briefly, 120 mL of CTAC was added to 600 mL of deionized water with stirring. Separately, a second solution was prepared by mixing 135 mL of TEOS with 108 mL of NH_4OH. This solution was then added to the CTAC solution, and the resulting mixture was covered with parafilm and stirred at room temperature for 1 h. The white precipitate formed was collected by filtration, washed three times with

https://doi.org/10.1021/acscatal.6c00096
ACS Catal. 2026, 16, 9887−9901

deionized water, and dried overnight at 80 °C. Finally, the dried sample was calcined at 550 °C for 5 h at a heating rate of 2 °C/min.

MCM-56 was prepared using a hydrothermal method. Deionized water, 50% NaOH solution, and $NaAlO_2$ were first combined in a beaker and mixed thoroughly. ULTRASIL VN 3 was then added, and the mixture was stirred until a homogeneous gel formed. HMI was subsequently added to the gel, and the mixture was stirred for a further 10 min before being transferred to a Parr autoclave. The autoclave was heated at 143 °C with stirring at 400 rpm for 36.5 h. The solid product was recovered by filtration, washed with deionized water, and dried overnight at 60 °C. Finally, a two-step calcination was performed: the sample was first calcined at 428 °C for 3 h under a nitrogen atmosphere with a heating rate of 2 °C /min, followed by calcination in air at 540 °C for 8 h using the same heating rate.

2.3. Catalyst Synthesis

All catalysts were prepared using a modified precipitation method. The appropriate amount of the nickel precursor to achieve a loading of 5 wt % was dissolved in 300 mL of deionized water under stirring at room temperature. To precipitate Ni^{2+} ions, a 1.0 M NaOH solution was added dropwise until the pH of 9.6 corresponding to the quantitative precipitation (estimated based on the solubility product value for nickel(II) hydroxide − $K_{sp}(Ni(OH)_2) = 5.48 \times 10^{-16}$) was reached. Subsequently, 1.5 g of the porous support was gradually introduced into the mixture while continuously monitoring and maintaining the pH by further addition of the NaOH solution as necessary. An ultrasonic homogenizer was then used to improve the dispersion of the support in the solution. The pH was rechecked, and additional NaOH was added if required. As the dispersion of some supports caused a drop in pH, it was important to monitor the pH throughout the precipitation step to prevent nickel ions from returning to the aqueous form. The resulting sample was separated by centrifugation, washed three times with deionized water, and dried overnight at 80 °C. Finally, the dried material was calcined in air at 550 °C for 4 h with a heating rate of 2 °C/min to obtain the NiO catalyst.

Calcined forms of the porous supports were used for the preparation of all catalysts, except for NiO/MCM-22(P), where the precursor MCM-22(P) was used instead. Although the pore-directing agent decomposes during calcination and MCM-22(P) is converted to MCM-22, the sample is referred to as NiO/MCM-22(P) throughout the manuscript to distinguish it from the sample prepared using the calcined form of MCM-22.

2.4. Characterization Methods

Powder X-ray diffraction (PXRD) patterns of the samples were recorded using a PANalytical X'Pert PRO diffractometer with a fully opened 100-channel X'Celerator detector Plus and Cu-Kα radiation with a wavelength of 1.5418 Å. PXRD patterns were collected in the 2θ range of 2–80° with a step size of 0.034° per 100 s. The obtained patterns were analyzed using HighScore Plus 4.9 and subsequently plotted with Origin 2018.

Nitrogen physisorption analysis was conducted using a Micromeritics ASAP 2020 instrument. Before the experiment, the samples were degassed under vacuum at 573 K overnight. Subsequently, N_2 adsorption−desorption measurements were performed at −196 °C.

Scanning electron microscopy (SEM) analysis was conducted using a Zeiss Supra 35 VP microscope equipped with an energy-dispersive spectrometer (Oxford Instruments). An aperture size of 30 μm and an electron high-tension voltage of 1.00 kV were used to analyze the surface morphology, while energy-dispersive X-ray spectroscopy (EDX) analysis was performed with an electron high-tension voltage of 20.0 kV.

Transmission mode scanning transmission electron microscopy (TSEM) analysis was performed using a field-emission scanning electron microscope (FE-SEM) Apreo 2S (Thermo Fisher Scientific, Netherlands), equipped with a STEM3 + detector and an Ultim Max 100 energy-dispersive spectrometer (Oxford, UK), at an accelerating voltage of 30 kV and a beam current of 13 pA. Samples were prepared by direct deposition on copper holey carbon TEM grids (EMR, USA).

Scanning transmission electron microscopy (STEM) measurements were performed using a JEOL JEM NEOARM-200F microscope operated at 200 kV. Samples were prepared by direct deposition on copper holey carbon TEM grids (EMR, USA). Images were collected in scanning mode using a JEOL annular dark-field (ADF) detector. Energy-dispersive X-ray spectroscopy (EDS) element distribution maps were acquired using a JEOL JED-2300 energy-dispersive X-ray analyzer.

Temperature-programmed desorption of ammonia (NH_3-TPD) experiments were conducted using a 3500 3Flex (Micromeritics). Powder samples were pretreated in a helium flow (50 mL/min) at 500 °C for 2 h, with a heating rate of 10 °C /min. The samples were then cooled to 50 °C at 90 °C/min in helium (50 mL/min) and held at this temperature for 5 min before exposure to a 1% of NH_3/Ar gas mixture (50 mL/min) for 2 h. Subsequently, the samples were degassed in helium (50 mL/min) for 1 h to remove residual physisorbed ammonia and finally heated to 500 °C at 10 °C/min in helium flow (50 mL/min). Peak deconvolution was performed using Fityk software. Calibration is described in the Supplementary Information (Figure S15, eqs S1 and S2).

Hydrogen temperature-programmed reduction (H_2-TPR) was carried out using a Microtrac BELCAT II chemisorber analyzer equipped with a quadrupole mass spectrometer BELMASS II-62 (Microtrac, Haan, Nordrhein-Westfalen, Germany). Before the measurements, the samples were pretreated in an argon flow (50 mL/min) at 120 °C for 1 h. The samples were then heated in a flow of 5.05% H_2 in argon (50 mL/min) up to 1000 °C for the NiO/MCM-36 sample and up to 800 °C for other samples, at a heating rate of 20 °C/min. Peak deconvolution of H_2 consumption profiles was performed using Fityk software. Calibration is described in the Supplementary Information (Figure S20, eqs S3 and S4).

2.5. Plasma Reactor Setup and Conditions

Plasma-assisted synthesis of ammonia was carried out using a coaxial dielectric barrier discharge (DBD) reactor. Figure 1 presents a schematic of the experimental setup. The reactor comprised a quartz tube with an inner diameter of 4 mm and a wall thickness of 1 mm, serving as the dielectric barrier. A stainless-steel mesh, 20 mm in length, was wrapped around the outer surface of the tube and acted

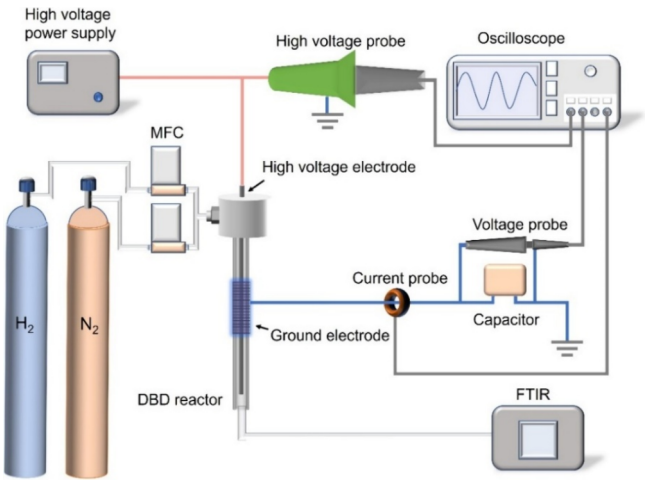

Figure 1. Schematic diagram of the plasma-assisted ammonia production system. Adapted from ref 47. Copyright (2025) American Chemical Society.

https://doi.org/10.1021/acscatal.6c00096
ACS Catal. 2026, 16, 9887−9901

as the ground electrode. A stainless-steel rod with a diameter of 2 mm was placed inside the tube to serve as the high-voltage electrode, creating a 1 mm discharge gap between the rod and the dielectric wall.

Plasma generation was driven by an AC sinusoidal high-voltage supply (maximum 30 kV peak-to-peak, frequency 11 kHz). The applied potential was monitored using a Tektronix P6015A high-voltage probe, while the voltage across the external capacitor (0.47 μF) was recorded with a Tektronix TPP0101 probe. The discharge current was measured with a Pearson 2877 current transformer, and the signals were simultaneously captured on a Tektronix MDO 3054 four-channel digital oscilloscope. The discharge power was quantified using the Q-U Lissajous method. For catalytic experiments, an average of 40 mg of the powdered NiO catalyst was packed into the discharge region, with a discharge length of 10 mm and a discharge volume of 0.38 cm^3, held in place on both sides with quartz wool. No reduction step was performed before the experiment. A feed gas mixture containing high-purity N_2 and H_2 was introduced at a combined flow rate of 40 mL/min and a ratio of 1:3. Finally, the gaseous product mixture was analyzed in real time by a Fourier-transform infrared (FTIR) spectrometer (Jasco FT/IR-4200). The reactor temperature was not actively controlled during operation but resulted solely from heating induced by the plasma discharge. The temperature was monitored using a thermal camera.[47]

3. RESULTS AND DISCUSSION

3.1. Catalyst Characterization

3.1.1. PXRD. The structural properties of the catalytic materials were examined using PXRD, N_2 physisorption, SEM, TSEM, and STEM. The PXRD diffraction patterns of MCM-22, MCM-36, and MCM-56 (Figure S1) show the typical MWW topology. A decrease in the intensity of the MCM-36 peaks compared to MCM-22 indicates the separation of MWW layers.[46,48]

In the pattern of MCM-56, broadening of the diffraction peaks is observed, indicating reduced crystallinity due to the layer disorder caused by delamination.[49] For the highly ordered mesoporous silica materials, a characteristic significant (100) peak at 2.3° for MCM-41[50] and a peak (211) at 2.7° for MCM-48[51] are present.

In the MCM-41 diffraction pattern, two well-separated additional characteristic peaks, (110) at 4.0° and (200) at 4.6°, can be identified, whereas the additional peaks of MCM-48 cannot be distinguished. The described structures are shown in Figure 2.

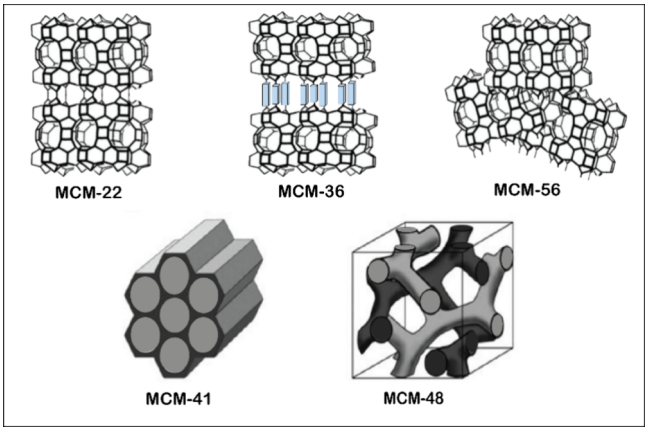

Figure 2. Schematic illustration of the structures of various MCM materials. Adapted from ref 52, available under CC-BY 4.0 license, copyright (2021) Erigoni and Diaz, and ref 45, available under CC-BY 4.0 license, copyright (2018) Schwanke and Pergher.

After loading the MWW zeolites with NiO, no significant decrease in the intensity of the peaks belonging to the support is observed. In contrast, there is a significant decrease in the intensity of the most distinct peaks for the mesoporous supports, indicating at least partial loss of long-range order, especially in the case of MCM-48. The diffraction peaks of NiO[20] at 37.2° (111), 43.3° (200), and 62.9° (220) are broad and have very low intensity (Figure S2), which might be attributed to poor crystallinity but is more likely caused by the very small particle size, as shown by bright field (BF) TSEM analysis (Figure 3).

3.1.2. N_2 Physisorption. Nitrogen physisorption isotherms and pore size distribution curves of the catalysts and pristine supports are shown in Figures S3 and S4. The isotherm of MCM-22 corresponds to a type I isotherm, reflecting the microporous nature of the material. The MCM-36 isotherm is similar to that of MCM-22, with a gradual increase in the amount of adsorbed nitrogen from a P/P_0 of 0.2 due to the presence of mesopores, created by pillaring with silica. This is usually described as a hybrid between type I and type IV isotherms.[46,48] This effect is even more pronounced in the case

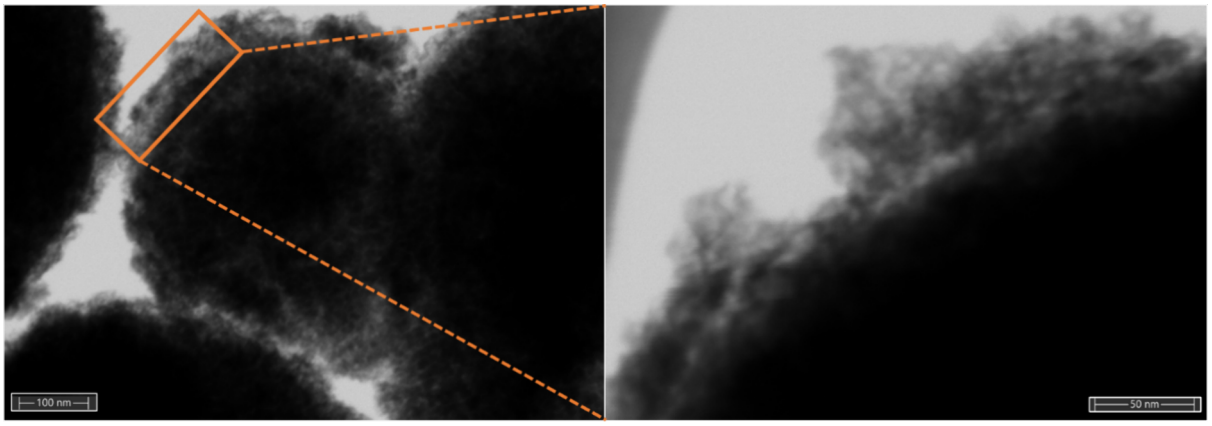

Figure 3. BF TSEM images of the NiO/MCM-48 catalyst at 350,000× (left) and 1000,000× (right) magnification.

https://doi.org/10.1021/acscatal.6c00096
ACS Catal. 2026, 16, 9887−9901

of MCM-56, where, in addition to the hybrid-type isotherm, a hysteresis loop is observed due to the more pronounced mesoporosity of the material and the presence of intercrystalline voids. The differences in the porous structure between the three tested pure MWW supports can be confirmed by the pore size distribution curves (Figure S3). An increase of the intensity of the peak at approximately 4 nm for MCM-36 compared to MCM-22 demonstrates the presence of mesopores, generated by the pillaring.[53] In the case of MCM-56, the peak intensity is even higher due to the disorder of the layers and the presence of intercrystalline voids.[54]

MCM-41 and MCM-48 exhibit a type IV(b) isotherm, typical of materials with smaller-width mesopores.[55] This is further demonstrated by the pore size distribution (Figure S4) showing high intensity peaks at 2.6 nm (MCM-41) and 2.5 nm (MCM-48). The specific surface areas and total pore volumes of the tested porous supports (Table S1) are consistent with the literature (MCM-22: 423–643 m^2/g and 0.4–0.5 cm^3/g,[46,48,56,57] MCM-36: 487–686 m^2/g and 0.2–0.8 cm^3/g,[48,58,59] MCM-41: 720–1240 m^2/g and 0.9−1.1 cm^3/g,[20,60−62] MCM-48: 652–1600 m^2/g and 0.31–1.32 cm^3/g,[63−66] MCM-56: 211–700 m^2/g and 0.2–0.5 cm^3/g.[43,49,58,67,68]

After loading the porous materials with NiO, three different effects on the specific surface area and total pore volume are observed. For MCM-36 and MCM-56 catalysts, there is a smaller decrease in the specific surface area, while no significant differences in total pore volume are detected. This may indicate that most NiO particles are located on the external or interlayer surfaces rather than within the pores of the microporous layers. Similarly, in pore size distribution curves, a decrease in the intensity of the peak at approximately 3.7 nm can be observed for both catalysts compared to the pure supports. For the NiO/MCM-36 catalyst, a broad shoulder in the existing peak ranging from 5 to 9 nm is present, indicating NiO in the pillared area and partial pore blockage. The location of NiO particles was further confirmed by H_2-TPR, as discussed in Section 3.4. The isotherm of NiO/MCM-36 shows a visible hysteresis loop, most likely caused by partial pore blockage by NiO. Compared to the pure supports, both the specific surface area and total pore volume of the NiO/MCM-41 and NiO/MCM-48 catalysts decrease significantly due to the mesopore blockage by NiO, evidenced by the hysteresis loop in the isotherms of both catalysts and by the shift of nitrogen adsorption towards higher relative pressure. This is also reflected in the pore size distribution curves (Figure S4), where a significant drop in the peak just under 3 nm and its shift towards smaller pore widths are apparent for both materials. In contrast, the surface area slightly increases after loading with NiO in both MCM-22 catalysts, which could be due to the separation of crystal agglomerates during the treatment. The same effect can be observed in the pore size distribution curves as the intensity of the peak at 4 nm even increases compared to the pure support.

3.1.3. Electron Microscopy. Scanning electron microscopy was conducted to examine the surface morphology of the samples. SEM images (Figures S5 and S6) show that MWW zeolites and their corresponding catalysts consist of MWW platelets with diameters of approximately 400 nm, forming homogeneous microspherical particles with diameters between 5 and 9 μm. In the cases of MCM-22 and MCM-36, the platelets are randomly oriented, displaying a typical dandelion-like morphology,[69] while the platelets in MCM-56 are thicker and more interconnected. Figure 4 shows the spherical morphology of MCM-41 and MCM-48 particles with diameters of roughly 400 nm. Some isolated spherical MCM-48 particles are observed, while MCM-41 particles are mostly agglomerated.

The differences between the structures of NiO catalysts are more clearly distinguished in the TSEM images obtained in high-angle annular dark-field (HAADF) mode (Figure S7). Catalysts supported by MWW zeolites exhibit a more compact structure with characteristically brighter, thicker layers, in contrast to MCM-41 and MCM-48 NiO catalysts. Furthermore, comparison of the SEM images of the NiO catalysts and pure supports (Figures 4 and S6) indicates no change in the supports' morphologies during the Ni precipitation process. NiO appears as an additional smaller domain on the otherwise smooth surface of the platelets. To obtain more detailed information on the morphology of NiO, STEM in annular dark-field (ADF) mode and STEM-EDS elemental mapping were used. As seen in Figure 5, NiO on the external surface is clearly visible due to the contrast in thickness between the NiO layer and the support. NiO is present as agglomerated and overgrown nanoplates with thicknesses of 1 nm as demonstrated by the embedded histogram in Figure 5b, forming a spider web-like layer on the surface of the porous support (Figure 3). Additionally, EDS elemental maps confirm that the layer of nanoplatelets belongs to NiO. Similar observations were made for all of the catalysts (Figure S8).

Additionally, elemental mapping based on scanning electron microscopy energy-dispersive X-ray spectroscopy (SEM-EDX) was used to determine the dispersion of NiO. Elemental mapping images (Figures S9−S14) demonstrate a mostly even dispersion of NiO, with the possible exception of a higher local NiO concentration at the contact points between two agglomerated support particles. SEM-EDX was also used to determine the loadings of NiO on the catalysts. The results are presented in Table S2.

3.2. Plasma-Catalytic Performance

To compare the catalytic performances of the materials in the DBD plasma-catalytic system, experiments were conducted at several discharge powers ranging from 4 to 10 W, while maintaining a constant total flow rate of 40 mL/min. Electrical diagnostics showed no significant influence on the plasma discharge properties after packing either pristine supports or any of the catalysts into the discharge region (Figures S21 and S22). Increasing the discharge power raised the ammonia concentration in both the plasma-only system and the packed systems (Figure S21), as more energetic electrons were produced, enhancing the generation of active species in the plasma region. However, increasing the number of energetic electrons leads to energy losses through ineffective collisions, gas heating, and enhanced ammonia dissociation, resulting in a decrease in energy yield (eq S5) at higher discharge powers (Figure S23).

Figure 6 presents the catalytic performances of the tested materials in relation to ammonia concentration. Compared with the plasma-only reaction, the use of pristine porous supports often significantly increases the amount of ammonia produced on account of the shielding effect and synergistic effect between plasma and the packed material. As previously reported, Figures S21 and S25 microporous materials can improve the efficiency of plasma-catalytic ammonia synthesis by promoting the diffusion of reactive species towards the active sites and into the pores. However, due to their reactivity and short lifetimes, the penetration of reactive species is limited to 1 μm.[22]

https://doi.org/10.1021/acscatal.6c00096
ACS Catal. 2026, 16, 9887−9901

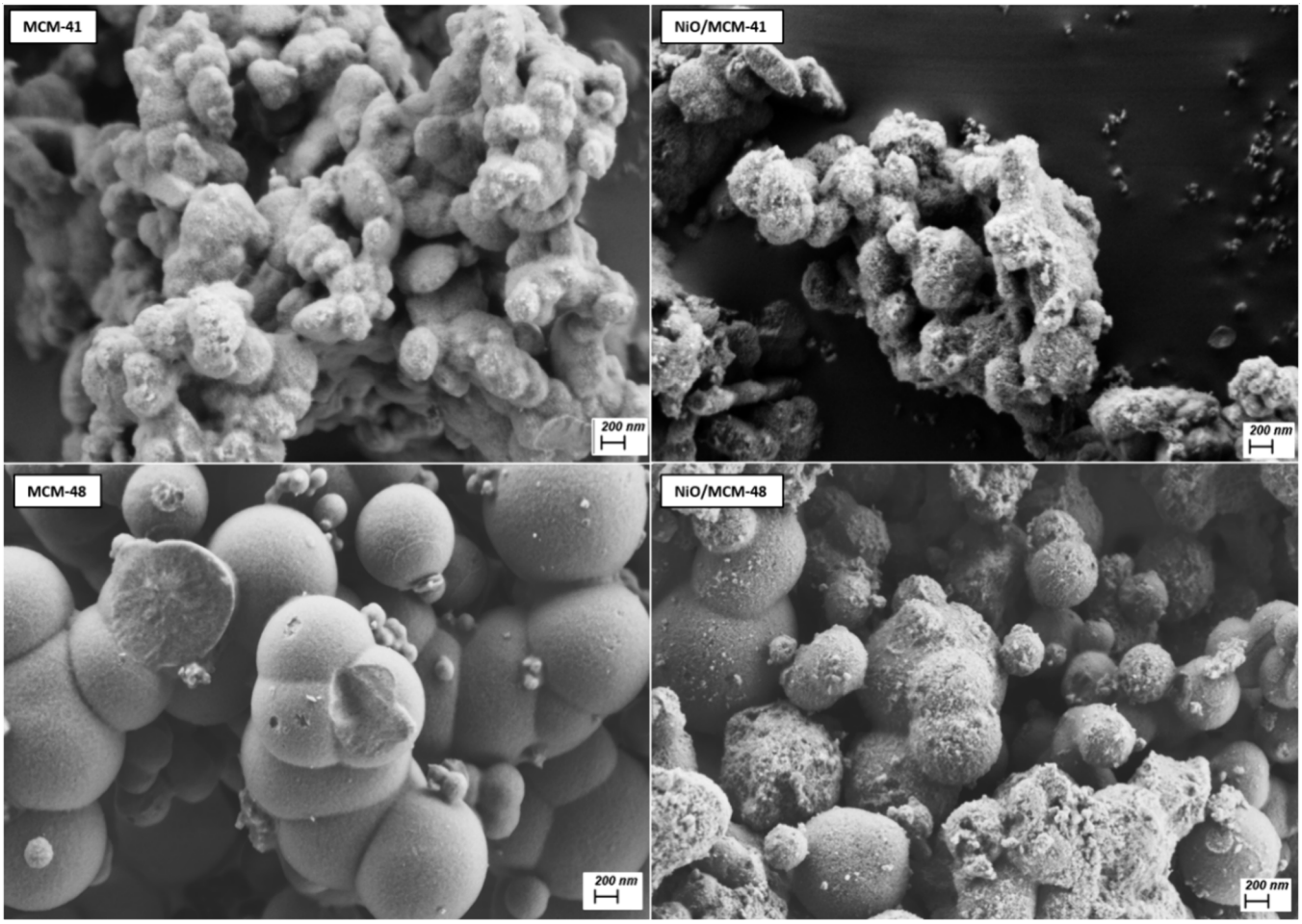

Figure 4. SEM images of MCM-41 (top left), NiO/MCM-41 (top right), MCM-48 (bottom left), and NiO/MCM-48 (bottom right) at 50,000× magnification.

The mesoporous silicas MCM-41 and MCM-48 exhibited the best performance, achieving up to approximately 300 and 260%, respectively, of the ammonia concentration observed in the plasma-only reaction under identical operating conditions. The MWW zeolites MCM-36 and MCM-22 also enhanced ammonia production, while MCM-56 performed worse than the plasma-only reaction.

We now turn to the catalyzed reactions with NiO-loaded supports, which generally perform better. At lower discharge power, NiO/MCM-48 was the best-performing supported NiO catalyst, yielding 2900 ppm of ammonia, which is approximately 420% of the plasma-only experiment. At 10 W, NiO/MCM-36 and NiO/MCM-41 showed the best performance, each yielding 4600 ppm of ammonia. Although the ammonia concentrations produced using these two materials were nearly identical, the ammonia reaction rate (eq S6) over NiO/MCM-41 reached 22.3 mmol h^{-1} g_{cat}^{-1}, approximately twice that observed over NiO/MCM-36.

Although it did not show the best catalytic performance overall, NiO/MCM-56 demonstrated the highest catalytic promotion by NiO, yielding approximately 390% of the ammonia concentration achieved using pristine MCM-56, while the best-performing catalysts reached only 110 to 160% of the ammonia concentration yielded by the pristine support. The highest energy yield of 1.2 g/kWh was achieved by NiO/MCM-48 at 4 W (Figure S24). These seemingly random trends are explained below, where we address how differences in acidity alter performance trends, how the function of acidic sites is dynamically verified, whether all porous materials exhibit a shielding effect, and how these effects act synergistically with NiO location.

3.3. Effect of Acidic Sites

The supports vary in the number and strength of acidic sites, which influences their catalytic performance. Zeolites can contain two types of acidic sites: Brønsted and Lewis. Brønsted acids are molecular entities that can donate a proton to a base or a corresponding chemical species. Substitution of Si^{4+} with trivalent Al^{3+} generates a negative charge within the framework, which requires compensation with a proton to maintain electroneutrality, generating Brønsted acidic sites. The proton is generally located at the oxygen atom of a bridging hydroxyl group between Si and Al. On the other hand, Lewis acids are molecular entities that can act as electron-pair acceptors and form Lewis adducts by sharing an electron pair with a Lewis base. In zeolites, Lewis acidic sites are related to coordinatively unsaturated Al^{3+}, such as extra-framework Al or framework tetrahedral Al atoms.[70−72]

The total surface acidity of the pristine supports and fresh catalysts was investigated by NH_3-TPD. The resulting profiles

https://doi.org/10.1021/acscatal.6c00096
ACS Catal. 2026, 16, 9887−9901

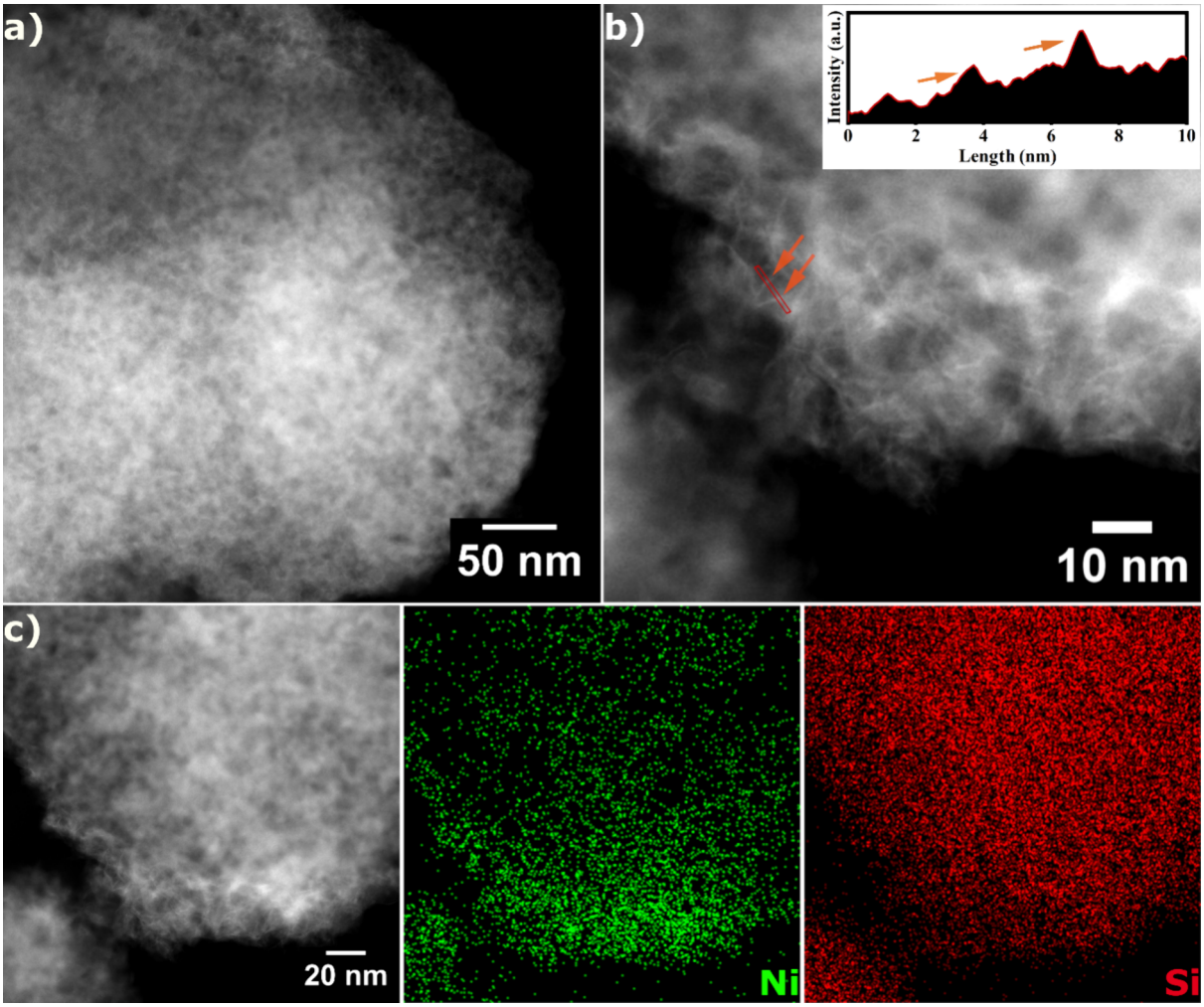

Figure 5. ADF-STEM images of the NiO/MCM-48 catalyst: (a) general view of the particle, (b) high-magnification image with visible NiO domains; the embedded histogram shows the thickness of layers indicated by orange arrows, and (c) STEM image with corresponding EDS elemental maps for Si (red) and Ni (green).

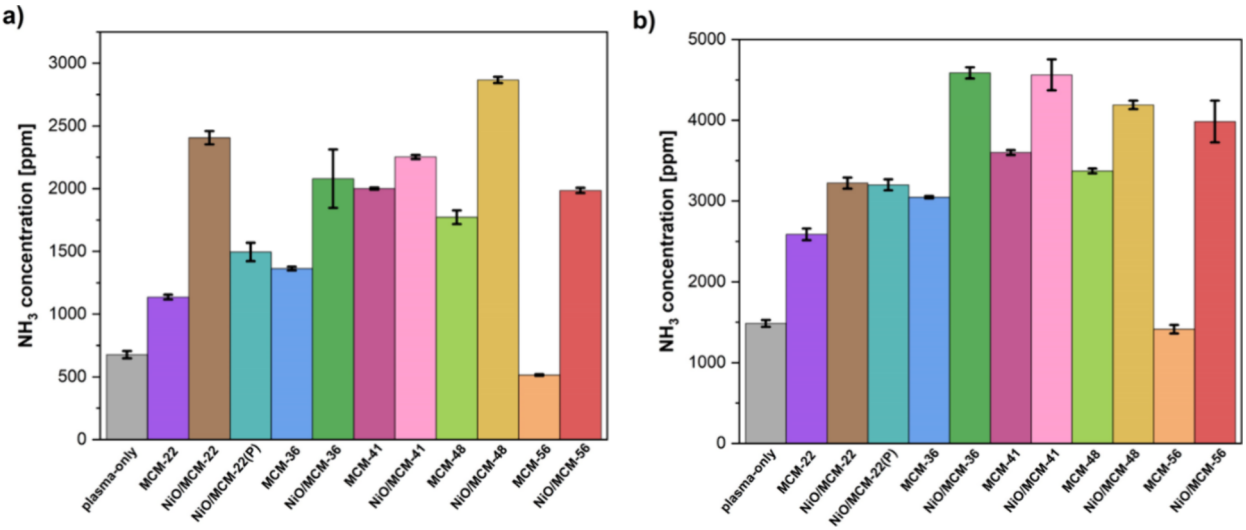

Figure 6. Ammonia concentrations in plasma-only and plasma-catalytic systems at (a) 4 W and (b) 10 W.

https://doi.org/10.1021/acscatal.6c00096
ACS Catal. 2026, 16, 9887−9901

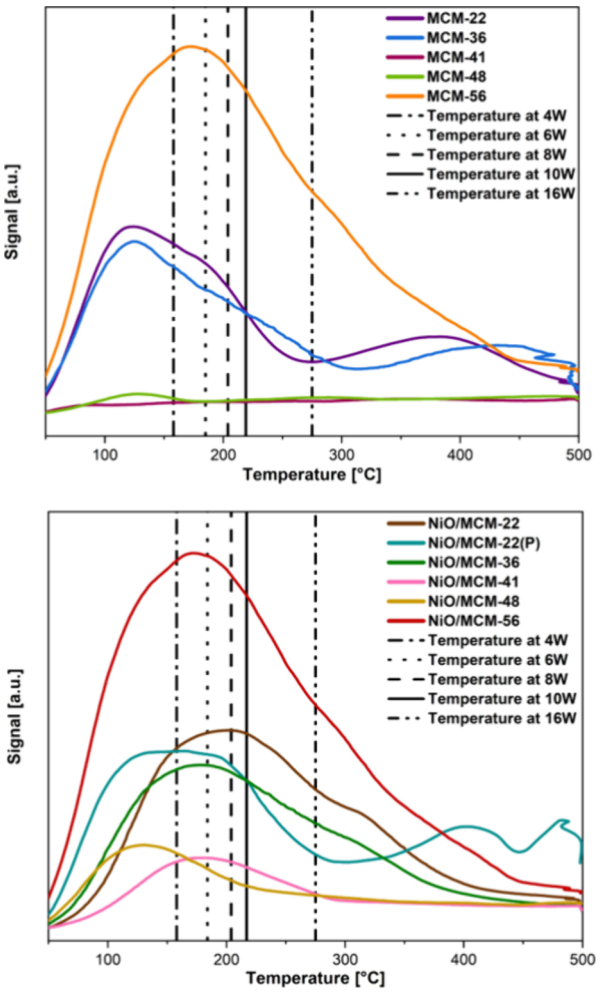

Figure 7. NH_3-TPD profiles of the pristine supports (top) and supported catalysts (bottom).

are shown in Figure 7, while the deconvoluted peaks are shown in Figures S16 and S17, with their corresponding temperatures presented in Table S3. Furthermore, the amount of acidic sites (Table S4) was determined based on the linear correlation between the peak area and the volume of consumed ammonia (Figure S15), as described in the Supplementary Information. It had been reported in the literature that MWW supports, highlighted in our research, contain both types of acidic sites[46,54,59,73] with dominating Brønsted sites.[46,59] However, based on NH_3-TPD alone, the specific type of acidic sites could not be determined. Therefore, the acidic sites were defined as weak, moderate, and strong, based on their ammonia desorption temperature. Weak acidic sites with TPD peaks at 180 °C correspond to physical adsorption, interaction with silanol groups, and possible weak Lewis sites. As the temperature in the DBD plasma reactor reached up to 210 °C, ammonia was easily desorbed from these acidic sites. On the other hand, weak to moderate Brønsted/moderate Lewis sites, considered as acidic sites with moderate strength, demonstrated desorption peaks in the temperature range of 180 to 350 °C. These acidic sites are strong enough to enable ammonia adsorption under the operating conditions, while still enabling the desorption without the need for a significant increase. Finally, strong Brønsted/moderate to strong Lewis sites, with desorption temperatures higher than 350 °C, provide strong ammonia adsorption.

As expected, pure mesoporous silicas MCM-41 and MCM-48 show either no ammonia desorption peak or only a negligible one, resulting from the structural defects.[70] This could explain the difference in activity of the mesoporous silicas compared to the MWW zeolitic materials. As no ammonia is adsorbed in MCM-41 and MCM-48, all produced ammonia leaves the system. In contrast, some ammonia may remain adsorbed on the moderate and strong acidic sites of the MWW zeolites, leading to lower detected concentrations of ammonia.

Even though MCM-36 and MCM-22 show similar NH_3-TPD profiles within the temperature range reached in the plasma reactor, the total acidity of MCM-36 (106 $\mu mol_{NH3}/g$) is lower compared to MCM-22 (124 $\mu mol_{NH3}/g$) due to the pillaring with silica, which could explain the better catalytic performance in the continuous power regime, in addition to its partial mesoporosity. Among the tested porous supports, MCM-56 has the highest number of acidic sites, with a total acidity of 249 $\mu mol_{NH3}/g$. Owing to its unilamellar structure, MCM-56 has a high concentration of external Brønsted acidic sites, corresponding to 12-ring half cavities on the surface,[59] which could explain the highest fraction (60.1%) of moderate sites among the tested pristine supports. At a discharge power of 10 W, the temperature in the plasma reactor reached 210 °C, at which only about 50% of ammonia is desorbed, based on the area under the TPD profile. Due to the higher number of acidic sites, the surface acidity of this material could more significantly influence the activity. The lower concentration of ammonia compared to plasma-only experiments could therefore be attributed to the acidity of the material. MCM-48, NiO/MCM-41, and NiO/MCM-48 exhibited a single desorption peak, and their deconvolution is not shown.

A clear difference between the two NiO/MCM-22 catalysts can be observed. When Ni^{2+} precipitation was performed using the MCM-22 precursor with the pore-directing agent still present in the structure, the surface acidity of the resulting catalyst is very similar to that of the pristine support with almost identical fractions of strong and weak acid sites. In contrast, when MCM-22 was used during the precipitation step, the acidic properties of the catalysts change significantly compared to pristine MCM-22. The weaker acidic sites shift towards higher desorption temperatures, which is reflected in a reduced fraction of weaker acidic sites and the appearance of a significant fraction (31.3%) of moderate acidic sites.

Loading MCM-36 with NiO has the greatest effect on the stronger acidic sites, as the clear desorption peak at approximately 400 °C is replaced by a peak at 370 °C, assigned to medium-strength acidic sites. For NiO/MCM-41 and NiO/MCM-48, a single desorption peak appears at 171 and 176 °C, respectively, which can be attributed to weaker Lewis acid sites related to nickel species or defects in the structure. In addition, the desorption peak at 353 °C present in the MCM-56 profile appears to split into two peaks at 304 and 446 °C in the case of NiO/MCM-56. The peak at 446 °C can be explained by the additional Lewis acid sites associated with NiO.[74,75]

While the total acidity of NiO/MCM-22 and NiO/MCM-36 remains similar to the pristine supports, there is a noticeable drop in total acidity of NiO/MCM-22P and NiO/MCM-56. As both of these catalysts contain the highest amount of NiO

https://doi.org/10.1021/acscatal.6c00096
ACS Catal. 2026, 16, 9887−9901

on the external surface of the support, this occurrence could be connected to interactions between Ni species and external Brønsted acidic sites. Similarly, Balcar et al.[73] reported a decrease in the concentration of Brønsted acidic sites after loading MCM-22 and MCM-56 with MoO_x species.

To utilize the catalytic promotion by NiO and the acidic properties of MCM-56 for potential sorption-enhanced plasma-catalytic ammonia synthesis, power-swing experiments were conducted using the previously described DBD reactor system. Rather than introducing external heating to desorb ammonia, the temperature inside the reactor was increased by increasing the discharge power, taking advantage of the short response times of plasma systems. At higher power, more electrical energy is supplied to the plasma and is mainly absorbed by electrons, which cause the gas heating through electron elastic collisions. For the power-swing experiment, the total flow rate was maintained at 40 mL/min with a N_2 to H_2 ratio of 1:3. Initially, the discharge power was set at 8 W for 30 min to achieve a stable ammonia concentration. The discharge power was then increased to 16 W to raise the temperature to 275 °C, enabling ammonia desorption. In the final step, the discharge power was reduced to 4 W to demonstrate possible ammonia readsorption. In addition to the NiO/MCM-56 catalyst, NiO/MCM-22, which has a moderate number of acidic sites, and NiO/MCM-41, with a very low number of acidic sites, were tested in the power-swing regime. The results are shown in Figure 8.

After increasing the discharge power to 16 W, a significant overshoot in ammonia concentration was observed when the reactor was packed with NiO/MCM-56, indicating the desorption of ammonia from the weak and moderate acidic sites of the catalyst that had been adsorbed during the first phase of the experiment. Additionally, a mirrored peak was observed during the transition from the second to the final phase, caused by the readsorption of ammonia. In contrast, the overshoot was very minor with NiO/MCM-22 and absent with NiO/MCM-41. Furthermore, the lack of the two mentioned peaks in a plasma-only experiment proves that the overshoot is not a consequence of the increase in discharge power. These results confirm that the poorer performance of NiO/MCM-56 compared to NiO/MCM-41, NiO/MCM-48, and NiO/MCM-36 in the continuous regime is due to the sorption of ammonia. Based on the results of the power-swing experiment, two different mechanisms can be observed. As NiO/MCM-41 contains a negligible amount of acidic sites, it enables only physical shielding of ammonia from dissociation in plasma, based on temporary pore confinement. Under the conditions presented, the ammonia residence time within the MCM-41 framework is therefore very short. In contrast, the moderate acidic sites of NiO/MCM-56 interact with ammonia, enabling its retention within the porous framework and demonstrating the sorption-enhanced mechanism (Figure 9). With increased temperature due to the increase in power, ammonia can then be recovered in the second phase of the experiment. Based on the NH_3-TPD profiles, only 50% of adsorbed ammonia is desorbed at 10 W, while approximately 74% is desorbed at 16 W. As demonstrated, the power-swing regime could be implemented for sorption-enhanced plasma-catalytic ammonia production as an alternative to the DBD plasma system combined with a thermal desorption step, as presented by Arumuganainar[26] and Rouwenhorst.[22]

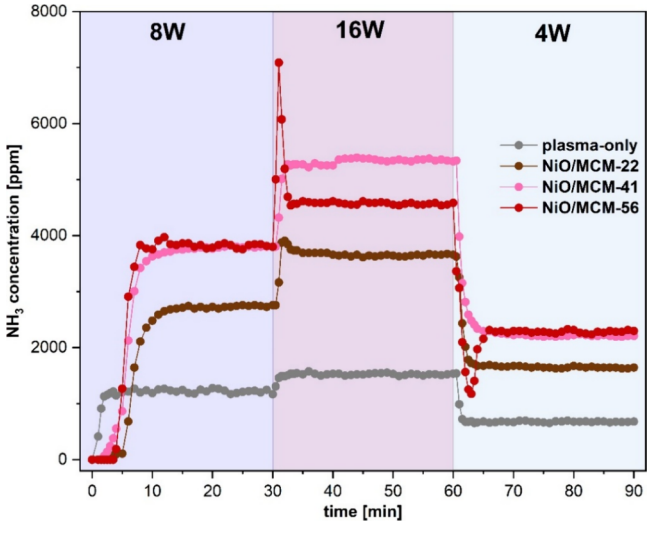

Figure 8. Ammonia concentration during the power-swing experiments.

The potential catalytic effect of acidic sites through the possible stabilization of reactive intermediates was studied using simple density functional theory (DFT) calculations described in the Supplementary information. It was determined that the interactions between acidic sites and NH, as well as N, are weak and short-lived, corresponding to non-specific van der Waals interactions. Consequently, the observed effect of the acidic sites is primarily related to the sorption and temporary storage of ammonia, rather than to a catalytic effect.

To show the stability under the employed conditions, the spent NiO/MCM-56 catalyst was characterized by XRD, SEM, and TSEM (Figures 10 and 11). By comparing the PXRD patterns of pristine and spent MCM-56 and NiO/MCM-56, no visible changes in crystallinity can be observed. In the pattern of spent NiO/MCM-56, the characteristic peaks of NiO remain visible with no significant changes in intensity or width, indicating no significant change in the particle size. Additionally, no peaks corresponding to metallic Ni are visible. A similar trend is observed for all tested catalysts (Figures S18 and S19).

Furthermore, SEM analysis showed that the typical morphology of MCM-56, consisting of interconnected platelets, is preserved without visible defects after exposure to plasma. NiO can still be seen as an additional domain on the surface of the support, while BF-TSEM images show that a thin layer of overgrown NiO nanoplates is preserved on the surface of the thicker, compact MWW layers of MCM-56.

3.4. Influence of Active Site Location and Porosity

To properly evaluate the shielding properties of the porous supports, both the adsorption strength of ammonia and its ability to diffuse into the pores, as well as its residence time within the framework, must be considered. However, since the temperature in our reactor system exceeds 100 °C even at the lowest discharge power, sustained confinement within the porous framework is limited, especially for pure MCM-41 and MCM-48, which have a negligible number of acidic sites, and MWW supports with weak acidic sites. Consequently, the purely physical pore confinement effect is expected to be weak under these reaction conditions. Therefore, the influence of the porous structure is primarily associated with the location of NiO, with the accessibility of the active sites to plasma-generated species becoming critically important. The location of the active phase

https://doi.org/10.1021/acscatal.6c00096
ACS Catal. 2026, 16, 9887−9901

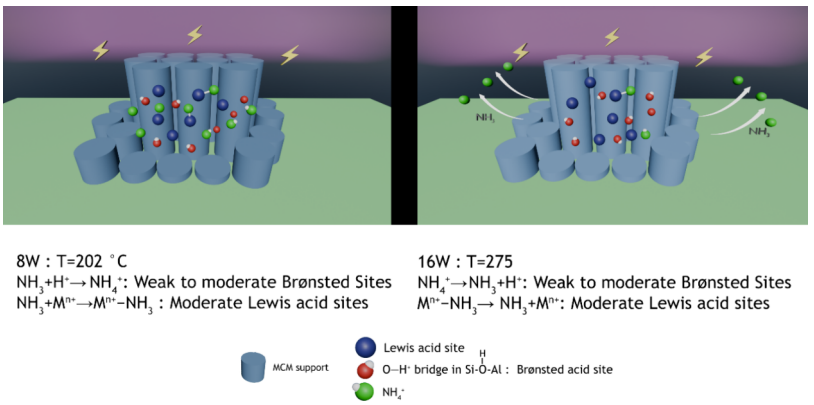

Figure 9. Schematic description of the sorption-enhanced mechanism during the power-swing experiment.

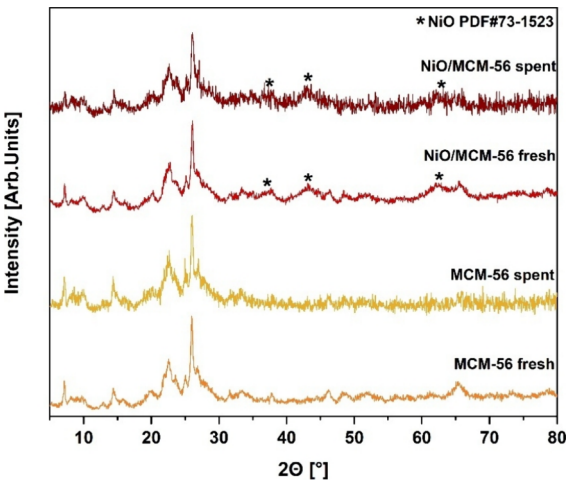

Figure 10. PXRD patterns of fresh and spent pristine MCM-56 and NiO/MCM-56.

has already been shown to influence the efficiency of plasma-catalytic ammonia production, especially when using a porous support. Wang et al.[20] demonstrated improved efficiency of the plasma-catalytic ammonia synthesis by designing a Ni/MCM-41 catalyst with Ni particles located mainly on the external surface area of the support, which enhanced plasma–catalyst interactions. To determine the location of NiO sites in the tested catalysts, H_2-TPR was employed. The H_2-TPR profiles and deconvoluted peaks are presented in Figure 12, while the temperatures of deconvoluted peaks are presented in Table 1. Due to the more complex structures of MWW zeolites compared to mesoporous silicas, the reduction peaks were divided into three main groups, as already suggested in the literature,[20] for easier comparison: NiO on the external surface of the support (α), NiO confined at the pore window or at contact points between 2 agglomerated support particles (β), and NiO inside the pores of the support (ɣ). Both NiO/MCM-22 and NiO/MCM-22(P) show two different α reduction peaks, which could be explained by the random orientation of the microporous platelets, causing some of the NiO particles to be located in the area between overlapping platelets, making them less exposed. Although the positions of the reduction peaks are similar for both NiO/MCM-22 catalysts, the percentage of total H_2 consumption (Table S5) for the reduction of α and β NiO is higher for NiO/MCM-22(P) (53% compared to 32% for NiO/MCM-22). This confirms that the use of the MCM-22 precursor in the metal precipitation phase leads to a supported catalyst with NiO particles better exposed to plasma, as the pore-directing agent partially prevents $Ni(OH)_2$ from accessing the pores of the support.

Due to the pillared structure of the support, the NiO/MCM-36 H_2-TPR profile shows two ɣ NiO reduction peaks. The first peak at 570.9 °C can be assigned to NiO located in the microporous layers, while the second peak at 721.4 °C can be assigned to NiO in the pillared area between the microporous layers. The two different types of ɣ NiO particles account for 88% of the total H_2 consumption. From the TPR profile of NiO/MCM-41, one reduction peak for each NiO type can be observed. Compared to MWW zeolites, the position of α NiO is shifted towards higher reduction temperatures. MWW zeolites contain Al, which interacts more strongly with NiO and consequently enables easier reducibility of NiO, shifting the reduction peak towards lower temperatures. Similar to NiO/MCM-36, ɣ NiO particles represent 76% of the NiO particles. In the case of NiO/MCM-48, the proportion of ɣ NiO is the highest among the tested catalysts at 98%. In the profile of NiO/MCM-56, two different β reduction peaks can be observed. One peak can be attributed to NiO at the entrance to the pores of the microporous layers, while the second can be attributed to NiO in the interlayer voids. Among all of the tested catalysts, NiO/MCM-56 has the largest proportion of α and β NiO particles at 68%. H_2-TPR results confirm the trend in catalytic promotion by NiO in the continuous experiments. As the NiO–plasma interaction is the strongest among the catalysts due to the exposure of NiO, the catalytic promotion by NiO is the highest in NiO/MCM-56. On the other hand, catalysts with mesoporous supports show the lowest catalytic promotion by NiO due to weak plasma–NiO interaction, as most of the active phase is located inside the micropores of the plate-like crystals of the support.

The results clearly demonstrate that the catalytic performance in plasma-catalytic ammonia production is governed by the combination of surface acidity, porous structure, and the location of the active phase, as summarized in Table 2. Catalysts supported on mesoporous materials with low total acidity (MCM-41 and MCM-48) exhibit superior performance under a typical continuous power regime. However, using a

https://doi.org/10.1021/acscatal.6c00096
ACS Catal. 2026, 16, 9887−9901

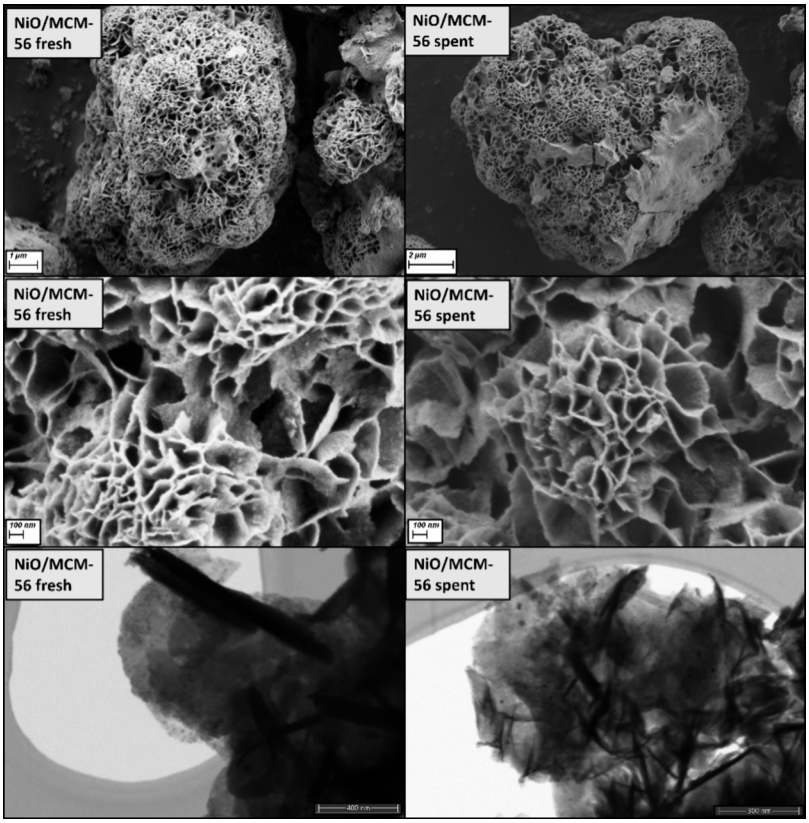

Figure 11. SEM (top and middle rows) and TSEM (bottom row) of fresh and spent NiO/MCM-56 catalysts.

catalyst with a high amount of moderate acidic sites and a large fraction of exposed active sites, such as NiO/MCM-56, combined with power-swing operation, can provide superior overall results. Even though, the temperature in a typical DBD plasma-catalytic system exceeds 100 °C, porous supports with optimal acidic properties still enable ammonia adsorption, reducing the probability of its dissociation in the plasma region and moving beyond the physical shielding of the porous material.

4. CONCLUSIONS

We aimed to systematically investigate the influence of porous supports on DBD plasma-catalytic ammonia synthesis. To this end, the activities of five different MCM materials were tested both as pristine supports and as supported NiO catalysts. The results showed that the supporting material affects catalyst activity through a combination of porous structure, active phase location, and surface acidity.

By comparing the activity of pristine supports in a typical continuous regime at fixed discharge power, the importance of surface acidity was demonstrated, as pure mesoporous silicas MCM-41 and MCM-48, with negligible acidic sites, outperformed the MWW zeolites. As MCM-56 contains more moderate-strength acidic sites, it adsorbed a significant portion of the produced ammonia. Under the applied conditions, less than 50% of the adsorbed ammonia was desorbed, leading to poorer performance compared to the plasma-only experiment. However, this property can be utilized to enhance the shielding effect, by adapting the operating conditions, as demonstrated by the power-swing experiments. By increasing the discharge power, the temperature inside the reactor increases, which enables ammonia desorption without the need for external heating, and thus utilization of the catalyst acidic properties for the shielding effect. Using a power-swing regime, NiO/MCM-56 achieved the highest peak concentration (7100 ppm) after desorbing additional ammonia adsorbed during the reaction at 8 W. This concentration is 1.5 times higher than that achieved by the best-performing catalysts among the materials tested in the continuous regime.

Although the NiO supported by the mesoporous supports showed the best overall activity for plasma-catalytic ammonia production, the promotion by NiO was the lowest among the tested materials due to poor interaction between the plasma and the active phase. Owing to the mesoporous structure, Ni^{2+} ions are more likely to migrate into the pores of the support during impregnation or precipitation, compared to microporous supports. This was also demonstrated by comparing the properties of NiO/MCM-22(P) and NiO/MCM-22 catalysts. Using the uncalcined MCM-22 precursor resulted in a larger portion of the active phase on the external surface and at the pore entrance, as well as different surface acidity. The importance of active phase location was clearly confirmed in the case of NiO/MCM-56, where the promotion by NiO was almost four times higher than that of the pristine support, achieving overall activity close to the best-performing catalysts.

Although the power-swing regime requires further optimization to improve energy efficiency, this research clearly demonstrates the potential of such a sorption-enhanced plasma-catalytic ammonia production system. More importantly, we showed that the catalytic performance is determined by porous structure, active phase location, and surface acidity.

https://doi.org/10.1021/acscatal.6c00096
ACS Catal. 2026, 16, 9887−9901

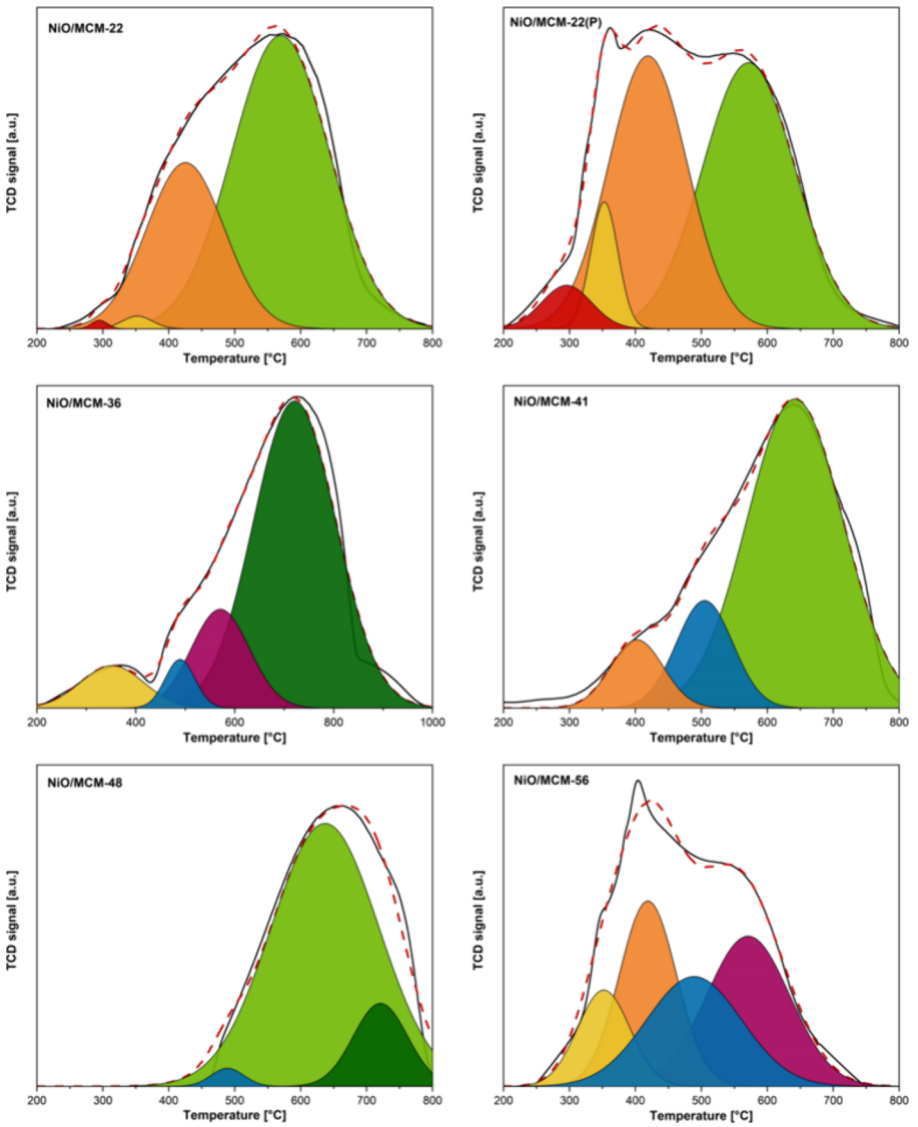

Figure 12. H_2-TPR profiles (black solid line), the fitted curves (red dashed line), and the deconvoluted peaks of the catalysts.

Table 1. Temperatures of the Deconvoluted H_2-TPR Peaks of the Catalysts

	peak temperature [°C]						
sample	α			β		γ	
NiO/MCM-22	295.1	352.2	425.5		569.9		
NiO/MCM-22(P)	295.9	352.9	419.0		571.8		
NiO/MCM-36		353.2		489.6	570.9		721.4
NiO/MCM-41		402.3		504.8		640.8	
NiO/MCM-48				489.1		637.2	721.0
NiO/MCM-56		352.2	419.2	489.0	571.2		

https://doi.org/10.1021/acscatal.6c00096
ACS Catal. 2026, 16, 9887−9901

Table 2. Summary Table of Important Properties of the Catalysts and Their Performances in Plasma-Catalytic Ammonia Synthesis

catalyst	S_{BET} [m^2/g]	V_{tot} [cm^3/g]	total acidity [μmol/g]	moderate acidity [μmol/g]	% of α + β NiO	c_{NH3} [ppm][a] 4 W	c_{NH3} [ppm][a] 10 W	$c_{max,NH3}$ PS [ppm][b]
NiO/MCM-22	535	0.5	129	40	32.4	2406	3227	3906
NiO/MCM-22(P)	510	0.5	100		52.3	2126	3222	
NiO/MCM-36	521	0.6	111	21	11.7	2079	4585	
NiO/MCM-41	548	0.6	35		24.5	2252	4562	5271
NiO/MCM-48	515	0.5	37		1.8	2867	4190	
NiO/MCM-56	361	0.6	219	159	67.5	1985	3984	7086

[a]Ammonia concentration during the continuous power experiment. [b]Maximum ammonia concentration during the power-swing experiment.

Therefore, an efficient catalytic material would have to optimize all of them simultaneously, while avoiding over-optimization of any single property.

■ ASSOCIATED CONTENT

Data Availability Statement

The data supporting this article have been included as part of the ESI.

Supporting Information

The Supporting Information is available free of charge at https://pubs.acs.org/doi/10.1021/acscatal.6c00096.

Fresh and spent catalyst characterization (PXRD, nitrogen physisorption, SEM, STEM, EDX, NH_3-TPD, H_2-TPR), electrical signal analysis and plasma diagnostics, plasma-catalytic results, preliminary DFT results (DOCX)

■ AUTHOR INFORMATION

Corresponding Authors

Xin Tu – *Department of Electrical Engineering and Electronics, University of Liverpool, Liverpool L69 3GJ, U.K.;* Email: xin.tu@liverpool.ac.uk

Blaž Likozar – *Department of Catalysis and Chemical Reaction Engineering, National Institute of Chemistry, Hajdrihova 19, Ljubljana SI-1001, Slovenia; Faculty of Chemistry and Chemical Technology, University of Maribor, Smetanova 17, Maribor 2000, Slovenia;* Email: blaz.likozar@ki.si

Matej Huš – *Department of Catalysis and Chemical Reaction Engineering, National Institute of Chemistry, Hajdrihova 19, Ljubljana SI-1001, Slovenia; University of Nova Gorica, Vipavska 13, Nova Gorica SI-5000, Slovenia; Association of Technical Culture of Slovenia, Zaloška 65, Ljubljana SI-1000, Slovenia;* Email: matej.hus@ki.si

Authors

Katja Vodlan – *Department of Catalysis and Chemical Reaction Engineering, National Institute of Chemistry, Hajdrihova 19, Ljubljana SI-1001, Slovenia; Faculty of Chemistry and Chemical Technology, University of Ljubljana, Večna pot 113, Ljubljana SI-1000, Slovenia*

Weitao Wang – *Department of Electrical Engineering and Electronics, University of Liverpool, Liverpool L69 3GJ, U.K.*

Michal Mazur – *Department of Physical and Macromolecular Chemistry, Faculty of Science, Charles University, Hlavova 8, Prague 128 00, Czechia;* orcid.org/0000-0001-5044-5284

Daria Sudakova – *Department of Physical and Macromolecular Chemistry, Faculty of Science, Charles University, Hlavova 8, Prague 128 00, Czechia*

Jens-Peter Baernholdt Haraldsted – *Danish Technological Institute, Gregersensvej 1, Taastrup 2630, Denmark*

Anej Blažič – *Department of Catalysis and Chemical Reaction Engineering, National Institute of Chemistry, Hajdrihova 19, Ljubljana SI-1001, Slovenia; University of Nova Gorica, Vipavska 13, Nova Gorica SI-5000, Slovenia*

Janvit Teržan – *Department of Catalysis and Chemical Reaction Engineering, National Institute of Chemistry, Hajdrihova 19, Ljubljana SI-1001, Slovenia;* orcid.org/0000-0001-5528-5355

Complete contact information is available at: https://pubs.acs.org/doi/10.1021/acscatal.6c00096

Notes

The authors declare no competing financial interest.

■ ACKNOWLEDGMENTS

The authors would like to thank Andraž Teržan for his help with Figure 9. This project received funding from the European Union's Horizon Europe research and innovation programme under grant agreement No 101083905 (DARE2X) and from UK Research and Innovation. Funding from the Slovenian Research and Innovation Agency (ARIS) is also acknowledged as core funding P2-0152, project funding J2-70085 (M.H.), and N2-0291 (B.L.). The research was co-funded under the HyBReED project, supported by the European Union—NextGenerationEU. Funding from the Ministry of Education, Youth and Sports of the Czech Republic is acknowledged for the ERDF/ESF grant TECHSCALE No. CZ.02.01.01/00/22_008/0004587(M.M.). D.S. and M.M. also acknowledge the Czech Science Foundation for Grant 23-08031K. The infrastructure obtained thanks through OP VVV "Excellent Research Teams", project no. CZ.02.1.01/0.0/0.0/15_003/0000417—CUCAM, was used in this study.

■ REFERENCES

(1) Gorky, F.; Best, A.; Jasinski, J.; Allen, B. J.; Alba-Rubio, A. C.; Carreon, M. L. Plasma Catalytic Ammonia Synthesis on Ni Nanoparticles: The Size Effect. *J. Catal.* **2021**, *393*, 369–380.

(2) Rouwenhorst, K. H. R.; Engelmann, Y.; van't Veer, K. ; Postma, R. S.; Bogaerts, A.; Lefferts, L. Plasma-Driven Catalysis: Green Ammonia Synthesis with Intermittent Electricity. *Green Chem.* **2020**, *22* (19), 6258–6287.

(3) Chen, X.; Jin, W.; Zhong, X.; Lin, H.; Ding, J.; Liu, X.; Wang, H.; Chen, F.; Xiong, Y.; Ding, C.; Jin, Z.; Jiang, M. Optimized Kinetic Pathways of Active Hydrogen Generation at Cu_2O/Cu Heterojunction Interfaces to Enhance Nitrate Electroreduction to Ammonia. *Chin. J. Catal.* **2025**, *79*, 78–90.
(4) Smith, C.; Hill, A. K.; Torrente-Murciano, L. Current and Future Role of Haber−Bosch Ammonia in a Carbon-Free Energy Landscape. *Energy Environ. Sci.* **2020**, *13* (2), 331–344.
(5) Fernández, C. A.; Chapman, O.; Brown, M. A.; Alvarez-Pugliese, C. E.; Hatzell, M. C. Achieving Decentralized, Electrified, and Decarbonized Ammonia Production. *Environ. Sci. Technol.* **2024**, *58* (16), 6964–6977.
(6) Yüzbaşıoğlu, A. E.; Avşar, C.; Gezerman, A. O. The Current Situation in the Use of Ammonia as a Sustainable Energy Source and Its Industrial Potential. *Curr. Res. Green Sustain. Chem.* **2022**, *5*, No. 100307.
(7) Carreon, M. L. Plasma Catalytic Ammonia Synthesis: State of the Art and Future Directions. *J. Phys. D Appl. Phys.* **2019**, *52* (48), 483001.
(8) Erisman, J. W.; Sutton, M. A.; Galloway, J.; Klimont, Z.; Winiwarter, W. How a Century of Ammonia Synthesis Changed the World. *Nat. Geosci.* **2008**, *1* (10), 636–639.
(9) Chatterjee, S.; Parsapur, R. K.; Huang, K.-W. Limitations of Ammonia as a Hydrogen Energy Carrier for the Transportation Sector. *ACS Energy Lett.* **2021**, *6* (12), 4390–4394.
(10) Iwamoto, M.; Akiyama, M.; Aihara, K.; Deguchi, T. Ammonia Synthesis on Wool-Like Au, Pt, Pd, Ag, or Cu Electrode Catalysts in Nonthermal Atmospheric-Pressure Plasma of N_2 and H_2. *ACS Catal.* **2017**, *7* (10), 6924–6929.
(11) Sun, B.; Mu, S.; Chen, B.; Hu, G.; Gao, R.; Shi, C. Hydrogen Production via Ammonia Decomposition on Molybdenum Carbide Catalysts: Exploring the Mo/C Ratio and Phase Transition Dynamics. *Chin. J. Catal.* **2025**, *74*, 365–376.
(12) Machaj, K.; Kupecki, J.; Malecha, Z.; Morawski, A. W.; Skrzypkiewicz, M.; Stanclik, M.; Chorowski, M. Ammonia as a Potential Marine Fuel: A Review. *Energy Strategy Rev.* **2022**, *44*, No. 100926.
(13) Portarapillo, M.; Bellucci Sessa, A.; Russo, D.; di Benedetto, A. Ammonia as a Hydrogen Carrier: Energetic Assessment of Processes Integrated with Fuel Cells for Power Generation. *Energy Fuels* **2025**, *39* (5), 2843–2853.
(14) Winter, L. R.; Chen, J. G. N_2 Fixation by Plasma-Activated Processes. *Joule* **2021**, *5* (2), 300–315.
(15) Bogaerts, A.; Centi, G.; Hessel, V.; Rebrov, E. Challenges in Unconventional Catalysis. *Catal. Today* **2023**, *420*, No. 114180.
(16) Gorbanev, Y.; Fedirchyk, I.; Bogaerts, A. Plasma Catalysis in Ammonia Production and Decomposition: Use It, or Lose It?. *Curr. Opin. Green Sustain. Chem.* **2024**, *47*, No. 100916.
(17) Hong, J.; Prawer, S.; Murphy, A. B. Plasma Catalysis as an Alternative Route for Ammonia Production: Status, Mechanisms, and Prospects for Progress. *ACS Sustain. Chem. Eng.* **2018**, *6* (1), 15–31.
(18) Hong, J.; Zhang, T.; Zhou, R.; Dou, L.; Zhang, S.; Zhou, R.; Ashford, B.; Shao, T.; Murphy, A. B.; Ostrikov, K. (Ken); Cullen, P. J. Green Chemical Pathway of Plasma Synthesis of Ammonia from Nitrogen and Water: A Comparative Kinetic Study with a N_2/H_2 System. *Green Chem.* **2022**, *24* (19), 7458–7468.
(19) Barboun, P. M.; Otor, H. O.; Ma, H.; Goswami, A.; Schneider, W. F.; Hicks, J. C. Plasma-Catalyst Reactivity Control of Surface Nitrogen Species through Plasma-Temperature-Programmed Hydrogenation to Ammonia. *ACS Sustain. Chem. Eng.* **2022**, *10* (48), 15741–15748.
(20) Wang, Y.; Yang, W.; Xu, S.; Zhao, S.; Chen, G.; Weidenkaff, A.; Hardacre, C.; Fan, X.; Huang, J.; Tu, X. Shielding Protection by Mesoporous Catalysts for Improving Plasma-Catalytic Ambient Ammonia Synthesis. *J. Am. Chem. Soc.* **2022**, *144* (27), 12020–12031.
(21) Shah, J R; Gorky, F.; Lucero, J.; Carreon, M. A.; Carreon, M. L. Ammonia Synthesis via Atmospheric Plasma Catalysis: Zeolite 5A, a Case of Study. *Ind. Eng. Chem. Res.* **2020**, *59* (11), 5167–5176.
(22) Rouwenhorst, K. H. R.; Mani, S.; Lefferts, L. Improving the Energy Yield of Plasma-Based Ammonia Synthesis with In Situ Adsorption. *ACS Sustain. Chem. Eng.* **2022**, *10* (6), 1994–2000.
(23) Gorky, F.; Nambo, A.; Carreon, M. A.; Carreon, M. L. Plasma Catalytic Conversion of Nitrogen and Hydrogen to Ammonia over Silico Alumino Phosphate (SAPO) Zeolites. *Plasma Chem. Plasma Process.* **2023**, *44*, 1357–1368.
(24) Shah, J.; Wu, T.; Lucero, J.; Carreon, M. A.; Carreon, M. L. Nonthermal Plasma Synthesis of Ammonia over Ni-MOF-74. *ACS Sustain. Chem. Eng.* **2019**, *7* (1), 377–383.
(25) Gorky, F.; Guthrie, S R; Smoljan, C. S.; Crawford, J. M.; Carreon, M. A.; Carreon, M. L. Plasma Ammonia Synthesis over Mesoporous Silica SBA-15. *J. Phys. D Appl. Phys.* **2021**, *54* (26), 264003.
(26) Arumuganainar, S. E.; Sartzetakis, S.; Hullfish, C. W.; Koel, B. E.; Sarazen, M. L. Influence of Ordered Mesoporous Oxides in Plasma-Assisted Ammonia Synthesis. *Energy Fuels* **2024**, *38* (23), 23150–23166.
(27) Chen, J.; Tang, T.; Wu, X.; Li, C.; Su, X.; Rac, V.; Rakić, V.; Du, X. Unlocking Efficient Synergistic Plasma-Catalyst Ammonia Synthesis: System Optimization and Catalyst Support Screening. *Energy Fuels* **2024**, *38* (11), 10345–10356.
(28) Gorky, F.; Carreon, M. A.; Carreon, M. L. Experimental Strategies to Increase Ammonia Yield in Plasma Catalysis over LTA and BEA Zeolites. *IOP SciNotes* **2020**, *1* (2), No. 024801.
(29) Zhang, Y.-R.; Van Laer, K.; Neyts, E. C.; Bogaerts, A. Can Plasma Be Formed in Catalyst Pores? A Modeling Investigation. *Appl. Catal. B, Environ.* **2016**, *185*, 56–67.
(30) Chen, Z.; Jaiswal, S.; Diallo, A.; Sundaresan, S.; Koel, B. E. Effect of Porous Catalyst Support on Plasma-Assisted Catalysis for Ammonia Synthesis. *J. Phys. Chem. A* **2022**, *126* (46), 8741–8752.
(31) Li, S.; Shao, Y.; Chen, H.; Fan, X. Nonthermal Plasma Catalytic Ammonia Synthesis over a Ni Catalyst Supported on MgO/SBA-15. *Ind. Eng. Chem. Res.* **2022**, *61* (9), 3292–3302.
(32) Rouwenhorst, K. H. R.; Kim, H.-H.; Lefferts, L. Vibrationally Excited Activation of N_2 in Plasma-Enhanced Catalytic Ammonia Synthesis: A Kinetic Analysis. *ACS Sustain. Chem. Eng.* **2019**, *7* (20), 17515–17522.
(33) Kim, H.; Teramoto, Y.; Ogata, A.; Takagi, H.; Nanba, T. Atmospheric-pressure Nonthermal Plasma Synthesis of Ammonia over Ruthenium Catalysts. *Plasma Process. Polym.* **2017**, *14* (6), No. 1600157.
(34) Akay, G. Sustainable Ammonia and Advanced Symbiotic Fertilizer Production Using Catalytic Multi-Reaction-Zone Reactors with Nonthermal Plasma and Simultaneous Reactive Separation. *ACS Sustain. Chem. Eng.* **2017**, *5* (12), 11588–11606.
(35) Herrera, F. A.; Brown, G. H.; Barboun, P.; Turan, N.; Mehta, P.; Schneider, W. F.; Hicks, J. C.; Go, D. B. The Impact of Transition Metal Catalysts on Macroscopic Dielectric Barrier Discharge (DBD) Characteristics in an Ammonia Synthesis Plasma Catalysis Reactor. *J. Phys. D Appl. Phys.* **2019**, *52* (22), 224002.
(36) Barboun, P.; Mehta, P.; Herrera, F. A.; Go, D. B.; Schneider, W. F.; Hicks, J. C. Distinguishing Plasma Contributions to Catalyst Performance in Plasma-Assisted Ammonia Synthesis. *ACS Sustain. Chem. Eng.* **2019**, *7* (9), 8621–8630.
(37) Xie, Q.; Zhuge, S.; Song, X.; Lu, M.; Ruan, R.; Nie, Y.; Ji, J. Hydrogenation of Plasma-Excited Nitrogen over an Alumina Catalyst for Ammonia Synthesis. *Int. J. Hydrogen Energy* **2018**, *43* (32), 14885–14891.
(38) Mehta, P.; Barboun, P.; Herrera, F. A.; Kim, J.; Rumbach, P.; Go, D. B.; Hicks, J. C.; Schneider, W. F. Overcoming Ammonia Synthesis Scaling Relations with Plasma-Enabled Catalysis. *Nat. Catal.* **2018**, *1* (4), 269–275.
(39) Shamzhy, M.; Gil, B.; Opanasenko, M.; Roth, W. J.; Čejka, J. MWW and MFI Frameworks as Model Layered Zeolites: Structures, Transformations, Properties, and Activity. *ACS Catal.* **2021**, *11* (4), 2366–2396.
(40) Lee, G.; Jang, E.; Lee, T.; Jeong, Y.; Kim, H.; Lee, S.; Chung, Y. G.; Ha, K.-S.; Baik, H.; Jang, H.-G.; Cho, S. J.; Choi, J. Effective Delamination of a Layered Two-Dimensional MCM-22 Zeolite: Quantitative Insights into the Role of the Delaminated Structure on Acid Catalytic Reactions. *Catal. Today* **2023**, *411–412*, 113856.

https://doi.org/10.1021/acscatal.6c00096
ACS Catal. 2026, 16, 9887−9901

(41) Wang, Y.; Zhang, Y.; Chu, W.; Gao, Y.; Xie, S.; Li, X.; Xu, L.; Zhu, X. Advances in the Green and Controllable Synthesis of MWW Zeolite. *Chem. Commun.* **2024**, *60* (73), 9907–9917.
(42) Grzybek, J.; Roth, W. J.; Gil, B.; Korzeniowska, A.; Mazur, M.; Čejka, J.; Morris, R. E. A New Layered MWW Zeolite Synthesized with the Bifunctional Surfactant Template and the Updated Classification of Layered Zeolite Forms Obtained by Direct Synthesis. *J. Mater. Chem. A* **2019**, *7* (13), 7701–7709.
(43) Korzeniowska, A.; Grzybek, J.; Kałahurska, K.; Kubu, M.; Roth, W. J.; Gil, B. The Structure-Catalytic Activity Relationship for the Transient Layered Zeolite MCM-56 with MWW Topology. *Catal. Today* **2020**, *345*, 116–124.
(44) Fabbiani, M.; Morsli, A.; Confalonieri, G.; Cacciaguerra, T.; Fajula, F.; Haines, J.; Bengueddach, A.; Arletti, R.; Di Renzo, F. On the Chemical Condensation of the Layers of Zeolite Precursor MCM-22(P). *Microporous Mesoporous Mater.* **2022**, *332*, No. 111678.
(45) Schwanke, A.; Pergher, S. Lamellar MWW-Type Zeolites: Toward Elegant Nanoporous Materials. *Appl. Sci.* **2018**, *8* (9), No. 1636.
(46) Marosz, M.; Samojeden, B.; Kowalczyk, A.; Rutkowska, M.; Motak, M.; Díaz, U.; Palomares, A. E.; Chmielarz, L. MCM-22, MCM-36, and ITQ-2 Zeolites with Different Si/Al Molar Ratios as Effective Catalysts of Methanol and Ethanol Dehydration. *Materials* **2020**, *13* (10), No. 2399.
(47) Sun, J.; Wang, W.; Lu, C.; Tu, X. Elevated Pressure Effects on Plasma-Driven Ammonia Synthesis: Insights from Experiments and Kinetic Modeling. *ACS Sustain. Chem. Eng.* **2025**, *13* (37), 15576–15587.
(48) Lacarriere, A.; Luck, F.; Świerczyński, D.; Fajula, F.; Hulea, V. Methanol to Hydrocarbons over Zeolites with MWW Topology: Effect of Zeolite Texture and Acidity. *Appl. Catal. A Gen.* **2011**, *402* (1–2), 208–217.
(49) Juttu, G. G.; Lobo, R. F. Characterization and Catalytic Properties of MCM-56 and MCM-22 Zeolites. *Microporous Mesoporous Mater.* **2000**, *40* (1–3), 9–23.
(50) Kruk, M.; Jaroniec, M.; Kim, J. M.; Ryoo, R. Characterization of Highly Ordered MCM-41 Silicas Using X-Ray Diffraction and Nitrogen Adsorption. *Langmuir* **1999**, *15* (16), 5279–5284.
(51) Solovyov, L. A.; Belousov, O. V.; Dinnebier, R. E.; Shmakov, A. N.; Kirik, S. D. X-Ray Diffraction Structure Analysis of MCM-48 Mesoporous Silica. *J. Phys. Chem. B.* **2005**, *109* (8), 3233–3237.
(52) Erigoni, A.; Diaz, U. Porous Silica-Based Organic-Inorganic Hybrid Catalysts: A Review. *Catalysts* **2021**, *11* (1), 79.
(53) Roth, W. J.; Kresge, C. T.; Vartuli, J. C.; Leonowicz, M. E.; Fung, A. S.; McCullen, S. B. MCM-36: The First Pillared Molecular Sieve with Zeoliteproperties. *Stud. Surf. Sci. Catal.* **1995**, *94*, 301–308.
(54) Li, A.; Zhang, X.-X.; Zhang, Y.; Shamzhy, M.; Guo, X.-Z.; Yan, W.; Li, B.; Hu, X.; Cai, R.; Zhou, F. Structural Dimensionality Governing CO_2/C_2H_2 Separation in MWW Zeolites. *Mater. Horiz.* **2026**, *13* (5), 2267–2274.
(55) Thommes, M.; Kaneko, K.; Neimark, A. V.; Olivier, J. P.; Rodriguez-Reinoso, F.; Rouquerol, J.; Sing, K. S. W. Physisorption of Gases, with Special Reference to the Evaluation of Surface Area and Pore Size Distribution (IUPAC Technical Report). *Pure Appl. Chem.* **2015**, *87* (9–10), 1051–1069.
(56) Chen, J.; Peng, G.; Liang, T.; Zhang, W.; Zheng, W.; Zhao, H.; Guo, L.; Wu, X. Catalytic Performances of Cu/MCM-22 Zeolites with Different Cu Loadings in NH3-SCR. *Nanomaterials* **2020**, *10* (11), 2170.
(57) Ahmad, A.; Naqvi, S R; Rafique, M.; Nasir, H.; Sarosh, A. Synthesis, Characterization and Catalytic Testing of MCM-22 Derived Catalysts for n-Hexane Cracking. *Sci. Rep.* **2020**, *10* (1), 21786.
(58) Gil, B.; Makowski, W.; Marszalek, B.; Roth, J. W. ; Kubu, M.; Čejka, J.; Olejniczak, Z. High Acidity Unilamellar Zeolite MCM-56 and Its Pillared and Delaminated Derivatives. *Dalton Trans.* **2014**, *43* (27), 10501.
(59) Jankowska, A.; Kowalczyk, A.; Rutkowska, M.; Mozgawa, W.; Gil, B.; Chmielarz, L. Silica and Silica−Titania Intercalated MCM-36 Modified with Iron as Catalysts for Selective Reduction of Nitrogen Oxides − the Role of Associated Reactions. *Catal. Sci. Technol.* **2020**, *10* (23), 7940–7954.
(60) Fenelonov, V. B.; Romannikov, V. N.; Derevyankin, A. Y. U. Mesopore Size and Surface Area Calculations for Hexagonal Mesophases (Types MCM-41, FSM-16, Etc) Using Low-Angle XRD and Adsorption Data. *Microporous Mesoporous Mater.* **1999**, *28* (1), 57–72.
(61) Kruk, M.; Jaroniec, M.; Sayari, A. Adsorption Study of Surface and Structural Properties of MCM-41 Materials of Different Pore Sizes. *J. Phys. Chem. B* **1997**, *101* (4), 583–589.
(62) Candela-Noguera, V.; Alfonso, M.; Amorós, P.; Aznar, E.; Marcos, M. D.; Martínez-Máñez, R. In-Depth Study of Factors Affecting the Formation of MCM-41-Type Mesoporous Silica Nanoparticles. *Microporous Mesoporous Mater.* **2024**, *363*, No. 112840.
(63) Schumacher, K.; Grün, M.; Unger, K. K. Novel Synthesis of Spherical MCM-48. *Microporous Mesoporous Mater.* **1999**, *27* (2–3), 201–206.
(64) Romero, A. A.; Alba, M. D.; Klinowski, J. Aluminosilicate Mesoporous Molecular Sieve MCM-48. *J. Phys. Chem. B.* **1998**, *102* (1), 123–128.
(65) Trongjitraksa, P.; Jantharasuk, A.; Jareewatchara, W.; Klinthongchai, Y.; Jongsomjit, B.; Praserthdam, P. Enhancement of the Thermal Stability for MCM-48 with Incorporation of Different Metals. *Microporous Mesoporous Mater.* **2023**, *354*, No. 112556.
(66) Yu, Q.; Zhuang, R.; Yi, H.; Gao, W.; Zhang, Y.; Tang, X. Application of MCM-48 with Large Specific Surface Area for VOCs Elimination: Synthesis and Hydrophobic Functionalization for Highly Efficient Adsorption. *Environ. Sci. Pollut. Res.* **2022**, *29* (22), 33595–33608.
(67) Cao, S.; Xiao, P.; Liu, Q.; Ge, Y.; Chen, Z.; Li, Z.; Gong, Y.; Yan, X.; Li, Z. Green and Stable Synthesis of MCM-56 Zeolite by Using Choline Chloride as Template. *Microporous Mesoporous Mater.* **2024**, *371*, No. 113088.
(68) Jiang, L.; Li, X.; Gong, Y.; Meng, X.; Zhang, L.; Zhai, Y.; Shang, S.; Meng, L. MCM-56 Stabilization Synthesis Using Auxiliary Tetraethylammounium Ions: Its Role to Inhibit Surface Si-O-Al Bridged Linkage and Retain Highly Delaminated Structure. *Microporous Mesoporous Mater.* **2020**, *302*, No. 110245.
(69) Schwanke, A.; Villarroel-Rocha, J.; Sapag, K.; Díaz, U.; Corma, A.; Pergher, S. Dandelion-Like Microspherical MCM-22 Zeolite Using BP 2000 as a Hard Template. *ACS Omega* **2018**, *3* (6), 6217–6223.
(70) Palčić, A.; Valtchev, V. Analysis and Control of Acid Sites in Zeolites. *Appl. Catal. A Gen.* **2020**, *606*, No. 117795.
(71) Busca, G. Acidity and Basicity of Zeolites: A Fundamental Approach. *Microporous Mesoporous Mater.* **2017**, *254*, 3–16.
(72) Ayrault, P.; Datka, J.; Laforge, S.; Martin, D.; Guisnet, M. Characterization of the Internal and External Acidity of H-MCM-22 Zeolites. *J. Phys. Chem. B* **2004**, *108* (36), 13755–13763.
(73) Balcar, H.; Kubů, M.; Žilková, N.; Shamzhy, M. MoO_3 on Zeolites MCM-22, MCM-56 and 2D-MFI as Catalysts for 1-Octene Metathesis. *Beilstein J. Org. Chem.* **2018**, *14*, 2931–2939.
(74) Kostyniuk, A.; Bajec, D.; Likozar, B. Catalytic Hydrogenation, Hydrocracking and Isomerization Reactions of Biomass Tar Model Compound Mixture over Ni-Modified Zeolite Catalysts in Packed Bed Reactor. *Renew. Energy* **2021**, *167*, 409–424.
(75) Kostyniuk, A.; Key, D.; Mdleleni, M. 1-Hexene Isomerization over Bimetallic M-Mo-ZSM-5 (M: Fe, Co, Ni) Zeolite Catalysts: Effects of Transition Metals Addition on the Catalytic Performance. *J. Energy Inst.* **2020**, *93* (2), 552–564.

https://doi.org/10.1021/acscatal.6c00096
ACS Catal. 2026, 16, 9887−9901